Science Advances
AAAS

Supplementary Materials for

Changing spatial distribution of water flow charts major change in Mars's greenhouse effect

Edwin S. Kite*, Michael A. Mischna, Bowen Fan, Alexander M. Morgan, Sharon A. Wilson, Mark I. Richardson

*Corresponding author. Email: kite@uchicago.edu

Published 25 May 2022, *Sci. Adv.* **8**, eabo5894 (2022)
DOI: 10.1126/sciadv.abo5894

This PDF file includes:

Supplementary Text

1. Geologic background.

Early Mars had rivers and lakes (e.g., *1*, and references therein) (Fig. S1) that were filled with liquid water (*51*). In this study, we use rivers that were fed by precipitation (rain and/or meltwater) (e.g., *4,* and references therein). On Mars, the channel heads for young rivers can, in many locations, be traced up to ridgelines (e.g., at 24.1°S 28.2°E, 22.7°S 73.8°E, 21.4°S 67.3°E, and 19.9°S 327.3°E). This is as expected for precipitation-fed runoff but inconsistent with spring discharge. Moreover, drainage density at some sites is much higher than expected for spring-fed streams, and it is difficult for spring-fed streams to incise into bedrock as is required to explain the Mars data (*52*). We do not distinguish between shallow subsurface flow (within topographic catchments) and overland flow. Both are fed by precipitation (rain or snowmelt), and so have similar implications for paleoclimate.

We omit from this study channels that were formed by catastrophic outbursts of subsurface water and we omit almost all features where there are arguments both for and against a groundwater origin (e.g., *53-54*). We do interpret as precipitation-fed a small number of deltas that were interpreted by ref. *55* as formed by groundwater discharge. However, because our results are robust to excluding all deltas, this difference in interpretation is not important for our conclusions.

Multiple lines of evidence show that river water on Mars 3.5-3.0 Ga was mostly not produced by the localized effects of asteroid impacts (e.g., *2, 11, 18, 56).* For example, river/lake sediments found within large impact craters frequently contain smaller prefluvial/synfluvial impact craters (*2*). In order for these craters to accumulate, a time interval between the formation of the host craters and the end of river activity of ≥0.2 Gyr is required (e.g., *11*). The lifetime of post-impact hydrothermal activity is very much shorter, precluding post-impact hydrothermal activity as the source for river water. Moreover, simulations of impact-induced precipitation predict ≲1 yr-duration wet climates, too brief to match data for <3.6 Ga rivers and lakes (e.g., *56*, and references therein). The energy source for surface runoff was not impact energy, but insolation, based on the N-S orientation preference that has been reported for <3.6 Ga fans (*18*). Insolation-controlled (not impact-controlled) alluvial fan formation is also supported by the strong latitude dependence of fan-hosting craters (Fig. 2). The alluvial fan deposits are up to 1.1 km thick (*11*), which is, at best, only marginally consistent with a direct impact trigger for fan-forming rivers. It remains possible that impacts indirectly triggered wet climates by activating a mechanism that trapped sunlight energy (for example, through low-albedo impact ejecta, or by activating a hysteresis in the climate system, or by releasing H_2, *57*). Some steep (>10°) young (<1 Gya?) fans that are too small (<10 km^2, usually <1 km^2) to be included in the Fig. 1b survey probably did result from the localized effect of asteroid impacts (e.g. *58*). Possible water sources for these fans include localized precipitation or fall-back of wet ejecta. Moreover, some asteroid impacts on Mars triggered melting or release of subsurface fluids (e.g., *59*), but these are easily distinguished from landforms formed by precipitation-fed rivers. We also omit from our survey young gullies, which might be formed by mass wasting (for example, of CO_2 ice; *60*).

Intense geothermal heating (*61*), or lava, can melt ice, but high runoff production rates (e.g., *62*) rule out geothermal meltwater as the source of runoff. Lava deposits are not found in the locations where valley networks and paleolakes are seen, with rare exceptions that are excluded from our databases.

Chronologic constraints: The >3.6 Ga Valley Networks are distinguished from <3.6 Ga rivers on the basis of crosscutting relationships, crater densities, and the degree of preservation of crater rims (e.g., *3*, *42*). The <3.6 Ga rivers were usually shorter, with less integration of drainage basins (*63*), and <3.6 Ga crater rim erosion is more concentrated into alcoves (e.g., *64*). Later periods of river-forming climate show spatially more restricted fluvial erosion, (i.e., shorter rivers), and fewer aqueous minerals, but with high rates of peak runoff production (*3*, *51*, *62*). In many places, an epoch of deep wind erosion stratigraphically separates >3.6 Ga rivers from <3.6 Ga rivers (e.g. *14*). On Mars, almost all mappable-from-orbit fans/deltas postdate the Valley Networks. Because of these and other differences it is generally straightforward to distinguish between Valley Networks and <3.6 Ga rivers. However, detailed study of one Valley Network suggests that it was incompletely reactivated during later wet events (*65*). The <3.6 Ga rivers date from the Late Hesperian and Amazonian (e.g., *3, 38*). The currently most widely used mapping between relative and absolute age (*66*), which is uncertain by up to ±1 Gyr, is Noachian epoch → pre-3.6 Ga, Hesperian epoch → 3.6-3.2 Ga, Amazonian epoch → post-3.2 Ga. Ref. *10* reports crater counts on Valley Networks that are consistent with Valley Network formation during a <0.2 Ga interval around the Noachian-Hesperian boundary.

2. Detectability-corrected surveys for presence/absence of rivers.

We used an existing Valley Network database (from *17*). Other global Valley Network databases compiled using other methods show the same Valley Network spatial distribution pattern, with only minor differences (e.g., *67*). Most Valley Networks formed >3.6 Ga (*10*); a small percentage of Valley Networks are young and those were excluded from our analysis using criteria described below.

Our new fans/deltas database (Fig. 1b) is described in ref. 18. Fan-shaped deposits were classified, based on the presence of an arcuate frontal scarp indicative of subaqueous deposition, as being either putative deltas or alluvial fans. The fan apex was marked as the location where MOLA-derived contours indicated a transition from convergent to divergent flow, and the fan toe defined as the minimum elevation along a profile that extends from the apex to the point that is furthest from the apex along the fan outline. Fan and catchment areas were mapped using CTX images and MOLA-derived gridded elevation data. Elevation values for both the fan and the catchment were obtained from the MOLA 128 pixel/degree Digital Elevation Model (DEM). In total, our fans/deltas database has 1468 fans and deltas, 392 outside craters and 1076 inside craters (with 320 unique fan and/or delta-hosting craters). The largest previous survey involved ≈65 fans (*68*). We excluded 110 "terraced" deltas from further analysis. This is because terraced fans have been hypothesized to result from rapid groundwater outbursts (*53*). We also excluded 560 fans/deltas with fan area < 10 km^2 for the reasons described above. With these exclusions, 854 fans and deltas remained. These exclusions turn out to not make a big difference to the results (Fig. S3c).

We corrected both databases for detectability bias (post-fluvial resurfacing). A geologic feature of a given relative age has low/no detection probability if the terrain was subsequently resurfaced

by a geologic unit of a younger relative age. Relative-age assignments were made using the United States Geologic Survey (USGS) Global Geologic Map of Mars (*69*) and also a lower-resolution map by ref. *70* on a 2-pixel-per-degree grid. For the Valley Network-era time slice, terrain not mapped as "Noachian" was masked out. Terrain mapped as "HN" (Hesperian/Noachian), e.g., Meridiani Planum, was also masked out. A small percentage of Valley Networks postdate ~3.6 Ga (*10, 17*) – these usually have fewer branches and are usually superposed on young volcanoes. In order to remove these contaminants, we used age assignments mapped by ref. *10* as well as more recent geologic mapping (*69*) to remove valleys that crosscut (and so postdate) Hesperian or Amazonian terrain. We removed Valley Networks in the following zones: 45-86°E / 45-65°S (Malea Planum), -150 to -86°E / 0-50°N (Alba Patera and high Tharsis), 120-180°E / 11-45°N (Elysium), and 75-97°E / 30-50°S (E. Hellas). The combination of these masking steps reduced the number of valley segments from 59419 to 53489. (For legibility, in Fig. 1a we only plot every 4th valley segment). Black dots in Fig. 1a show segments inside our masked-out zone. Most valley segments are part of a larger valley network (n = 9879, of which 9278 survive our masking). For Fig. 2, when calculating error bars, we used the $\sqrt{N}$ error associated with the number of valley networks. For each valley segment, the location of a point roughly halfway along that segment (mean segment length = 12 km) was taken to be representative of the latitude and longitude of the segment. Using these coordinates, valley segment elevation was assigned using 8-pixel-per-degree MOLA data (*71*). Valley Networks are underrepresented in Arabia Terra due to erosion, burial, and the inverted-relief preservation style of fluvial materials in this region (e.g., *17*, *72*). Therefore, we excluded from our Valley Network analysis the region where abundant inverted river deposits are found, but few or no river valleys are found (*72*) (Fig. S8). Our conclusions turn out to be unaffected by this decision (Fig. S4). For the analysis of <3.6 Ga features, we masked out only terrain mapped by ref. *70* as either "Early Amazonian Vastitas Borealis Unit" or as "Late Hesperian – Late Amazonian volcanic materials". Although our post-fluvial resurfacing correction corrects for most of the detectability bias in our dataset, some post-fluvial processes can compromise the detection of fluvial features without fully resurfacing the landscape. Specifically, geologic features poleward of 40° in both hemispheres can be obscured by Amazonian slope-softening processes (*73*), and terrain at < -6 km elevation is on the Hellas basin floor, which has enigmatic geology. Our results are robust to the exclusion of these areas.

After masking, in order to make Fig. 2, the non-masked area (km^2) falling into every 2D elevation+latitude bin was calculated (Fig. S5). Also, the number of the corresponding geologic features falling into each 2D bin was calculated. In the case of Valley Network segments, segment frequencies were weighted by valley segment length. The outputs were marginalized on elevation or latitude. Then, the ratio of feature frequency to non-masked terrain area was taken to calculate relative frequency (units of km/km^2 for Valley Networks, and features/km^2 for fans). The resulting relative frequency histograms were normalized such that the area under each curve was unity (Fig. 2). Our inference of latitude-dependent Valley Network formation (Fig. 2) is supported by independent measurements of valley depth (*74*). Mean valley depth declines from ~140 m within 10° of the equator to ~110 m further (10-30°) from the equator (*74*).

The detection of a decline in the elevation of rivers over geologic time is robust to different choices about which elevations to plot. Sensitivity tests for different elevation-assignment choices are shown in Figs. S2-S3. A decline in the elevation of rivers over geologic time is seen

regardless of whether we use fan apex elevation, fan toe elevation, or maximum catchment elevation for fans/deltas, and regardless of whether we set the minimum Strahler order for Valley Networks to 1 or 3 (Fig. S4).

Post-fluvial tectonics was likely minor: Mars lacks plate tectonics and the amplitude of post-valley-networks True Polar Wander (TPW) was insufficient to produce the faulting pattern predicted for TPW (*75*). <3.6 Ga rivers show a distribution that parallels latitude bands, inconsistent with large-amplitude TPW after the <3.6 Ga rivers (Fig. 1b). Post-Valley-Network resurfacing (gray area in Fig. 1a) is the main cause for the >3.6 Ga Valley Networks showing a distribution that is roughly sinusoidal with longitude. A small-circle-fitting algorithm was applied by ref. *20* to the distribution of Valley Networks, and a paleopole at 69°N 118°W was proposed; however, this workflow neglected resurfacing. We applied this algorithm to a synthetic dataset in which, by construction, there is no polar wander, and found roughly the same paleopole (Fig. S7). Specifically, ref. *20* fits a small circle to the observed distribution of Valley Networks, assuming that the Valley Networks originally formed in a latitude belt that has been distorted by TPW into the observed roughly-sinusoidal shape (Fig. 1a). We applied the same TPW-retrieval procedure to synthetic data in which the distribution of Valley Networks is spatially uniform – i.e., by construction the synthetic data contain zero evidence for TPW (Fig. S7). Before running the paleopole-retrieval algorithm, we crudely implemented post-fluvial resurfacing by removing valleys in areas greatly affected by glacial resurfacing (poleward of 55°), in Arabia Terra (diagonal cut in center of Fig. S7), and in tectonized areas in Acheron and Tempe Terra (affected by faults such as Mareotis and Tempe Fossae). Ref. *20* (their Figure 1) does not show any valleys in Xanthe Terra, or SE of Argyre. For consistency with Figure 1 in (*20*), we also removed valleys in these regions, even though Noachian valleys in Xanthe Terra and SE of Argyre are mapped in ref. *17* (their Figure 1). The paleopole obtained by fitting a small circle to the synthetic data surviving this masking procedure is 79°N 122°W. The Valley Network-based paleopole reported by ref. *20* is 69°N 118°W (Fig. S7). These values are similar (Fig. S7), demonstrating the importance of correcting for subsequent resurfacing before application of the small-circle-fitting procedure of ref. *20* to Valley Network-era geologic data. Ref. *20* does not make such a correction, and on the basis of our calculation we believe that such a correction is a necessary step before making the claim that the Valley Network distribution is evidence for TPW on Mars (*20*).

Although it was once thought that the deviation of putative Mars Northern Ocean shorelines from an equipotential might be evidence for TPW, improved calculations from the same research group show that "Tharsis-induced TPW has a negligible effect" on the deviation of putative Mars Northern Ocean shorelines from an equipotential (*76*). Moreover, putative Mars Northern Ocean shoreline features have been questioned based on high-resolution data. If half or more of Tharsis was emplaced before the Valley Networks, then the theoretical upper limit on Tharsis-induced TPW is small, <9° (*76*). There is no need to appeal to TPW to explain the local lack of Valley Networks in E. Noachis (around 40°E 30°S) because this lack can be explained as due to a standing wave in the atmospheric circulation forced by ancient topography (e.g., *21,* and references therein). If large-amplitude (~20°) post-Valley Network TPW did, in fact, occur on Mars, our conclusion that Valley Networks formed at high elevation (Fig. 2) would be unaffected.

Light-toned, layered sedimentary rocks: Another geologic proxy for past near-surface liquid water that also postdates the Valley Networks is the distribution of light-toned layered

sedimentary rocks (*29, 77*). The water for aqueous cementation of these materials could have been supplied in the context of diagenesis by groundwaters, not necessarily surface flows (e.g., *14*). This proxy shows a low-elevation preference and strong latitude dependence, consistent with the shifting controls on river distribution. Fig. S6 shows the distribution of light-toned, layered sedimentary rocks as cataloged by ref. *77*. For a more inclusive catalog showing a broader distribution of sedimentary rocks, see *78.*

3. Global climate model (GCM) simulations.

Description of global climate model simulations.

In order to explore how patterns of temperature and snowpack stability change as a function of pCO_2 and of gray gas forcing, we used the MarsWRF GCM (*24*). The vertical grid uses a modified-σ (terrain-following) coordinate system with 40 vertical resolution levels. Periodic boundary conditions in the horizontal dimensions are employed, and an absorbing ("sponge") upper boundary condition was used. CO_2 radiative transfer uses a correlated-*k* scheme (*79*). A central aim of this study is to decouple the effect of loss of CO_2 from the effect of non-CO_2 greenhouse warming. To represent the non-CO_2 greenhouse warming, we use a gray gas approach (e.g., *25-26*). A well-mixed gray gas with adjustable absorption coefficient can approximate the effect of many potential non-CO_2 Mars warming agents (e.g., H_2, CH_4). For example, although cloud coverage on Earth is far from complete, water ice cirrus clouds can only provide strong greenhouse warming on Mars if cloud coverage is close to complete (e.g., *80*).

The dynamical time step varies between simulations (in the range 30 s – 180 s). The surface layer flux parameterization scheme is a Monin-Obukhov scheme. We assume pCO_2 is approximately equal to total atmospheric pressure; Mars's atmosphere is 95% CO_2 today, and atmosphere evolution calculations indicate that CO_2 was also the dominant constituent of the atmosphere in the past. Total atmospheric pressure would increase by <20% due to leading candidate agents of non-CO_2 greenhouse warming (H_2, CH_4, and high-altitude water ice clouds). We allow CO_2 ice clouds to form and we permit CO_2 seasonal polar cap condensation. We imposed: present-day topography (from MOLA; *71*), spatially uniform surface albedo (0.2) except when (CO_2) ice is on the surface, spatially uniform surface thermal inertia (250 J m^{-2} K^{-1} $s^{-½}$), and no atmospheric water cycle nor atmospheric dust. "Dust continents" (high-elevation, high-albedo, low-thermal-inertia zones) are omitted because their formation age is unknown and these "dust continent" features might postdate all of the fluvial features in our databases. Mars's geologic record of river forming climates spans 2 Gyr, and almost certainly samples multiple orbital states due to chaotic obliquity variations (e.g., *33*). Therefore, we carried out all our runs at both low (25°) and high (45°) obliquity. Eccentricity was set to zero, and all calculations were performed at 80% of present-day solar luminosity (as appropriate for ~3 Gya).

GCMs are run until the annual cycle has converged (typically <10 simulated years), at fixed orbital conditions. Output was sampled 260 times per year, allowing good sampling of the diurnal cycle in each season while preventing time-of-day aliasing (Fig. S9). Future studies might include more frequent output to fully resolve each diurnal temperature cycle, allowing direct computation of degree-days above freezing and meltwater production. The potential sublimation rate, S_{pot}, is defined as the sublimation that would be experienced by snow/ice if that snow/ice were forced to have the same temperature as simulated for bare ground; it is a measure

of relative snowpack stability (low potential sublimation rate = greater likelihood of snow accumulation; *25*, *29*). Details of how this is calculated are provided later in this Supplementary.

To check the precision of our model, we analyzed the energy conservation properties of our runs. In steady-state, ignoring energy uptake and release by the ground, annually-integrated and planet-averaged absorbed solar radiation equals annually-integrated outgoing longwave radiation. Averaging over the last year of the model run, the best-fit 20-mbar runs have an energy imbalance of <2.5 W/m^2, the best-fit 500-mbar runs have an energy imbalance of 5.1-6.2 W/m^2, and the best-fit 150-mbar runs (which are also the best overall fits shown in Figs. 3-4) have an energy imbalance of 2.3-3.0 W/m^2. This is sufficient for the purposes of our study.

The simplified meltwater model.

To get from the GCM model output to predicted meltwater runoff locations, we used a simplified meltwater model. The model assigns snow/ice to pixels that are calculated to have relatively low sublimation rate. Then, the model outputs a melt prediction for pixels where the temperature is warm enough for runoff (guided by terrestrial experience and ref. *30*, we choose a continuous 100-sol period with an average temperature >273 K for this threshold). The approach has been used before (*29*) and is consistent with Early Mars GCM output (*25*). The major advantages of the simplified meltwater model are: (i) hydrologic-cycle uncertainties are collapsed into a single parameter, f_{snow} (the fraction of the planet that has warm-season snow; small f_{snow} corresponds to patchy snow, and large f_{snow} corresponds to very extensive snow), (ii) fast runtime, and (iii) ease of downsampling to the smaller-than-GCM-pixel scale of the features of interest. When used in combination with the parameters used for the GCM-run ensemble, the simplified meltwater model also has restrictions and limitations: by construction, the model does not explicitly simulate rainfall (*19*, and references therein), we are not considering variations in orbital eccentricity, mesoscale processes such as orographic precipitation and steep slopes, nor the increase in solar luminosity during the period of river-forming climates on Mars. The flat albedo means that we are effectively assuming dusty snow (*40*).

Pressure, temperature T_{surf}, and wind speed $|u|$ for each of the 260 time steps in final-year model output are downsampled onto an 8 ppd topographic grid based on Mars Orbiter Laser Altimeter topography. In order to do this, the temperature is corrected for the adiabatic lapse rate (Fig. S12). The pressure is assumed to be a function of topography (a constant scale height of 10.7 km is assumed), but not time or latitude. The lapse rate is calculated by linear regression of the average temperature on the topography for latitudes <30°. The corresponding lapse-rate-based temperature offset is applied uniformly to get downsampled temperature as a function of time.

The warm season temperature at each of 2880 × 1440 pixels, $T_{warmseason}$, is calculated by finding the warmest 100-sol-average temperature (with a cyclic wrap). We assume $T_{warmseason} > 273$ K is required for runoff. This is a more stringent constraint than just producing some meltwater at the surface, which is appropriate because runoff requires thermal maturation of the snowpack to prevent refreezing during infiltration (*30*), and this choice is conservative.

The potential sublimation, S_{pot}, is calculated in post-processing as the sum of the potential forced sublimation and the potential free sublimation. The maximum annually integrated sublimation potential was calculated using the bare-ground temperature, combining the forced turbulent flux and free turbulent flux, assuming planetary boundary layer relative humidity of 50%. The potential free sublimation, S_{free}, (kg/m^2/s) is calculated as in refs *29* and *81*:

$$D_a = 1.387 \times 10^{-5} \, (T_{surf} / 273.15)^{1.5} \, (10^5/P) \quad (1)$$

$$v_a = 1.48 \times 10^{-5} \, (8.314 \, T_{surf} /(0.044 \, P)) \, ((240 + 293.15)./(240 + T_{surf})) \, (T_{surf} /293.15)^{1.5} \quad (2)$$

$$e_{sat} = 611.2 \exp(2834000 / 461.5 \, (1/273.16 - 1/ T_{surf})) \quad (3)$$

$$\rho_{sat} = e_{sat} /(R_{H2O} \, T_{surf}) \quad (4)$$

$$\rho_a = P / (8.314 / 0.044 \, T_{surf}) \quad (5)$$

$$\Delta\eta = \rho_{sat} \, (1\text{-}0.5) / \rho_a \quad (6)$$

$$\Delta\rho/\rho = (0.044\text{-}0.018) \, e_{sat} \, (1\text{-}0.5) / ((0.044 \, P)) \quad (7)$$

$$S_{free} = 1.57 \times 0.14 \times \Delta\eta \;\; \rho_a \, D_a \, ((v_a./D_a) \, (g/v_a^2) \, (\Delta\rho/\rho))^{1/3} \quad (8)$$

where D_a is diffusivity, v_a is kinematic viscosity, R_{H2O} is the specific gas constant for water, $g = 3.7$ m/s^2 is Mars gravity, and we have assumed that the boundary layer temperature, $T_{bl} \approx T_{surf}$. The forced potential sublimation S_{forced} (kg/m^2/s) is calculated as

$$S_{forced} = C_D \, |u| \, e_{sat} \, (1\text{-}0.5) /(R_{H2O} \, T_{surf}) \quad (9)$$

where C_D is the drag coefficient, set to a fixed value of 0.00275 (following ref. *25*). (Note that interpolation of wind speeds, shown in Fig. S13, onto high-resolution topography cannot represent slope-wind effects.) It is questionable whether the free and the forced sublimation should be summed together. In the case of this study, our choice to sum the loss mechanisms to get the total potential sublimation rate does not matter much because the forced sublimation turns out to dominate for the best-fit GCMs. The 2880 × 1440 × 260 grid of S_{pot} values is then annually averaged. The annual-averages are sorted to find the lower and higher values of S_{pot}, and each pixel is tagged with a value, f_{sub}, between ~0% (most favorable percentage of surface area for snow accumulation) and $f_{sub} \approx 100\%$ (least favorable percentage of surface area for snow accumulation). The pixels are cosine-corrected for latitude when doing this interpolation. Cold places are the most favorable for snow accumulation, which occurs below a threshold f_{snow}.

Comparing the results of the simplified meltwater model to geologic data.

For each of 100 values of f_{snow} from 1% to 100%, we calculate the predicted melt distribution by finding which pixels satisfy $T_{warmseason} > 273$ K and also $f_{sub} < f_{snow.}$ This gives 5400 forward models to be compared to each of the two time slices of data (early stage rivers and late stage rivers).

The model predictions and the data are spatially masked as described earlier (Fig. 1). Valley networks and fans are binned on an 8 ppd grid. Every pixel containing the center of a valley segment (for >3.6 Ga rivers) or a fan apex (for <3.6 Ga rivers) is assigned as a geologic positive, all other pixels are assigned as a geologic negative. The data are compared to the forward models and the numbers of true positives TP (model+, data+), false positives FP (model+, data-), true negatives TN (model-, data-), and false negatives FN (model-, data-) are calculated. These numbers are cosine-weighted for latitude correction. Metrics for assessing data-model agreement include

- *sensitivity*, the proportion of +ve cases correctly predicted, sensitivity = TP / (TP + FN). (Also known as *recall.*)
- *specificity,* proportion of -ve cases correctly predicted, specificity = TN / (TN + FP).
- *precision,* the fraction of model-predicted positives that are true positives, precision = TP/(TP+FP).

For each of the 54 GCM simulations, we marginalize over the 100 possible values of f_{snow} by plotting two of the above characteristics against each other, varying f_{snow}, and then computing a summary statistic. Specifically, for each of the 54 GCM simulations, we calculate a Receiver-Operating Characteristic (ROC) curve varying f_{snow} and measuring the area under the curve (AUC) of a plot of sensitivity against (1-specificity); informedness (Youden's J statistic, ref. *82*); and the precision-recall area-under-curve, PR-AUC). By varying f_{snow} over the full range, we weight all values equally. This is appropriate given ignorance of Early Mars hydrology, but future GCM work with coupled hydrology might motivate truncating at (for example) f_{snow} = 25%. Here we provide details on each summary metric. In practice AUC is calculated using the trapezium rule

$$\mathrm{AUC} = \Sigma_i \left[(\mathit{sensitivity}_i + \mathit{sensitivity}_{i+1}) / 2 \times (1\text{-}\mathit{specificity})_{i+1} - (1\text{-}\mathit{specificity})_i \right] \quad (10)$$

$$\mathrm{YoudensJ} = \max(\mathit{sensitivity} - (1 - \mathit{specificity})) \quad (11)$$

$$\text{PR-AUC} = \Sigma_i \left[(\mathit{precision}_i + \mathit{precision}_{i+1}) / 2 \times (\mathit{recall}_{i+1} - \mathit{recall}_i) \right] \quad (12)$$

Our procedure penalizes false positives and false negatives equally. However, an ideal early Mars climate model should have almost no false negatives. This is because (after geologic masking) our river maps are reliable, so false negatives are unlikely to be the result of mapping errors. By contrast, a false positive might be the result of local geologic circumstances de-linking runoff from river incision (e.g., large grain size making sediment transport, and thus landscape modification, difficult). However, penalizing false negatives more harshly than false positives would add an extra adjustable parameter (the punishment ratio) to the model, justifying our omission of this effect.

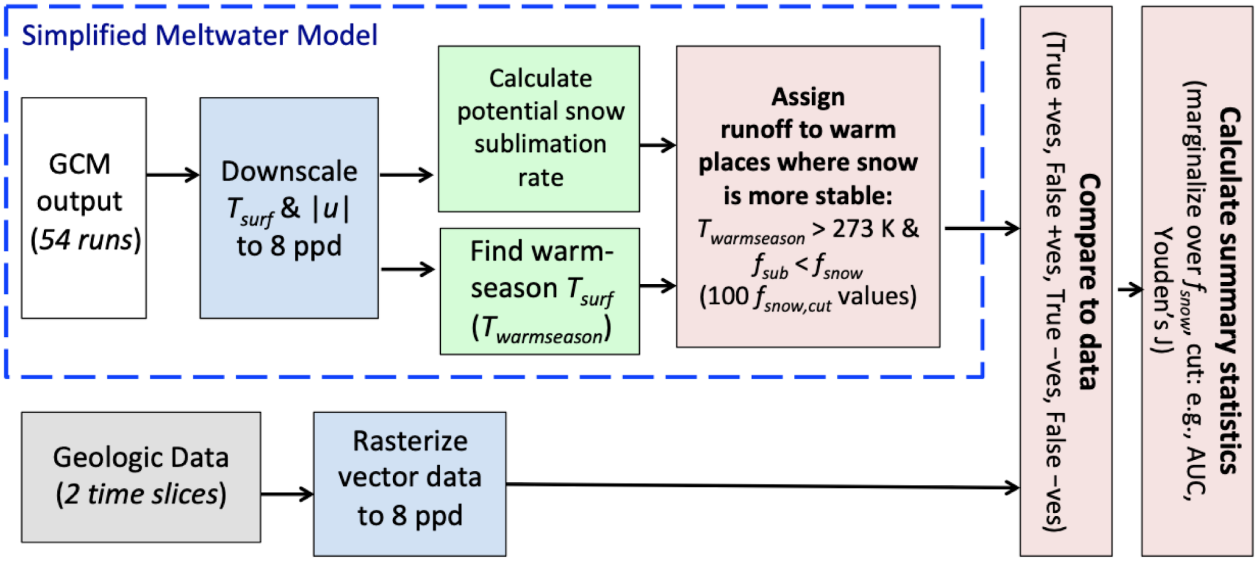

Fig. S1. Overview of data-model comparison. Explanation of variables: T_{surf} corresponds to surface temperature, $|u|$ corresponds to surface wind speed, $T_{warmseason}$ corresponds to the T_{surf} of the warmest season, f_{sub} corresponds to the favorability of the pixel for snow accumulation (f_{sub} = 10% means that only 10% of planet surface area is more favorable), and f_{snow} corresponds to the fraction of planet surface area with snow or ice during the warm season.

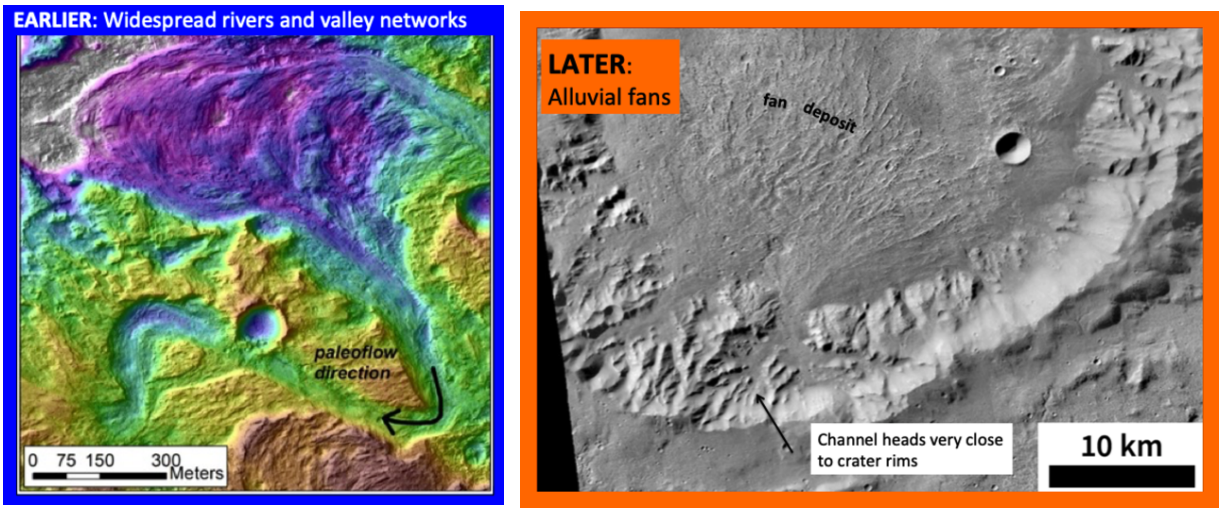

(a) **(b)**

Fig. S2. Examples of **(a)** well-preserved fluvial deposits from the Valley Network era (154.64°E 5.37°S), and **(b)** an alluvial fan (location from *11*).

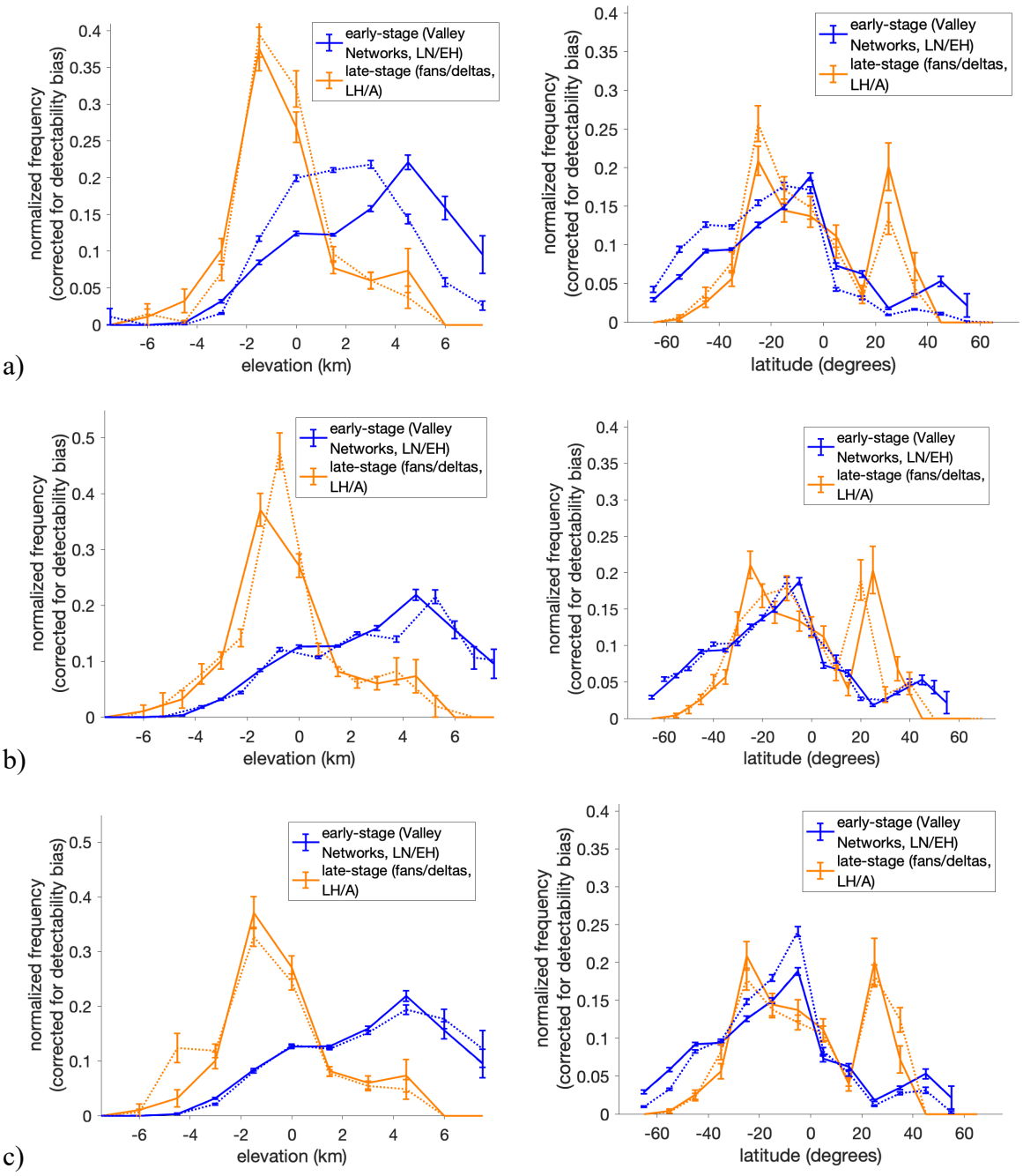

Fig. S3. Sensitivity tests for results shown in Fig. 2. Arabia Terra is not excised. **(a)** Uncorrected data shown in dotted lines, debiased data with solid lines. **(b)** Effect of bin offsetting. Dotted lines are with bin offsetting (by ½ bin width), and solid lines are with bins as shown in Fig. 2. **(c)** Solid blue lines: counting Valley Network segment number, instead of weighting by length. Dotted orange lines: 1 km^2 cut on the alluvial fans/deltas (instead of 10 km^2) and not excising terraced fans. Solid blue/orange lines: as in Fig. 2 (Valley Networks weighted by length, 10 km^2 cut on fan/delta size, terraced fans excised).

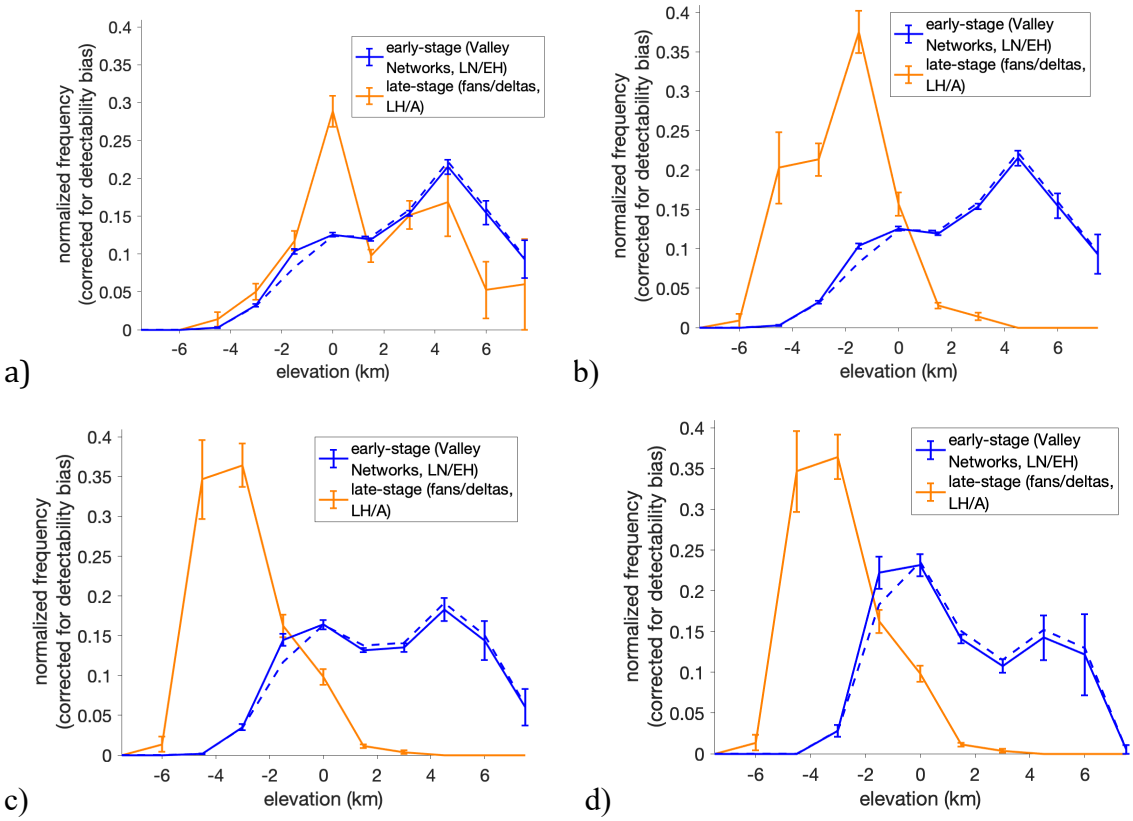

Fig. S4. Further sensitivity tests for elevation trends over time. **(a)** Maximum elevation within catchment for fans/deltas, vs. elevation of Valley Network valleys of all Strahler orders (this is not an apples-to-apples comparison, as catchment maximum elevation will overstate the elevation of typical channel heads). **(b)** Fan apex elevation vs. elevation of Valley Network valleys of all Strahler-orders. **(c)** Fan toe elevation vs. elevation of Valley Network valleys of Strahler orders 2 and higher ("trunk" streams). **(d)** Fan toe elevation vs. Strahler orders 3 and higher. Dashed lines correspond to the (small) effect of not excising Arabia Terra.

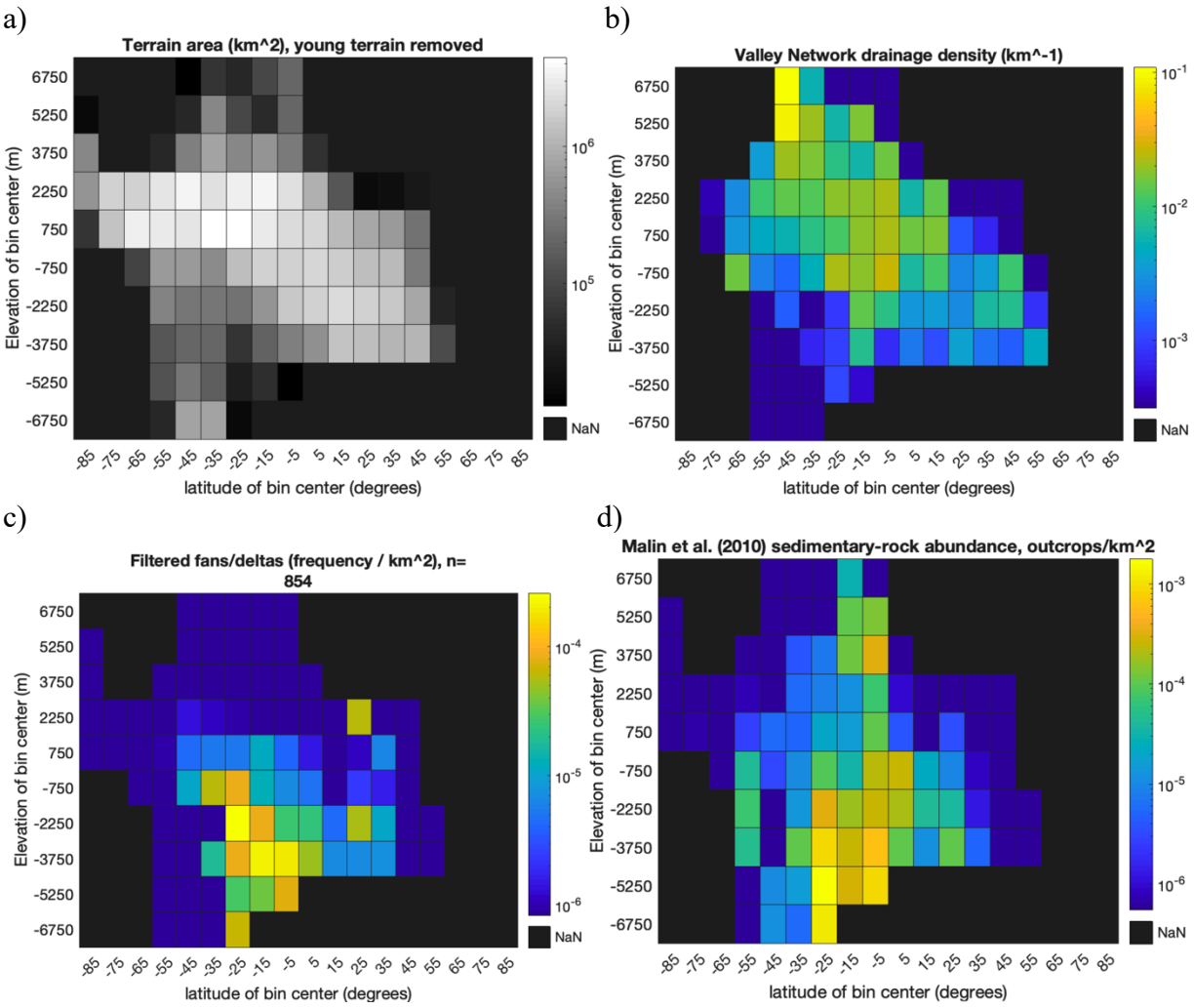

Fig. S5. Elevation+latitude distribution of **(a)** non-young terrain (excluding the masked-out area shown in Fig. 1b), **(b)** Valley Networks, **(c)** alluvial fans/deltas, and **(d)** light-toned, layered sedimentary rocks. Late stage latitude dependence is not an artifact of latitude-dependent hyposometry. For this figure only, elevation+latitude pixels with area < 10^4 km^2 are not shown (as they tend to be statistically noisy).

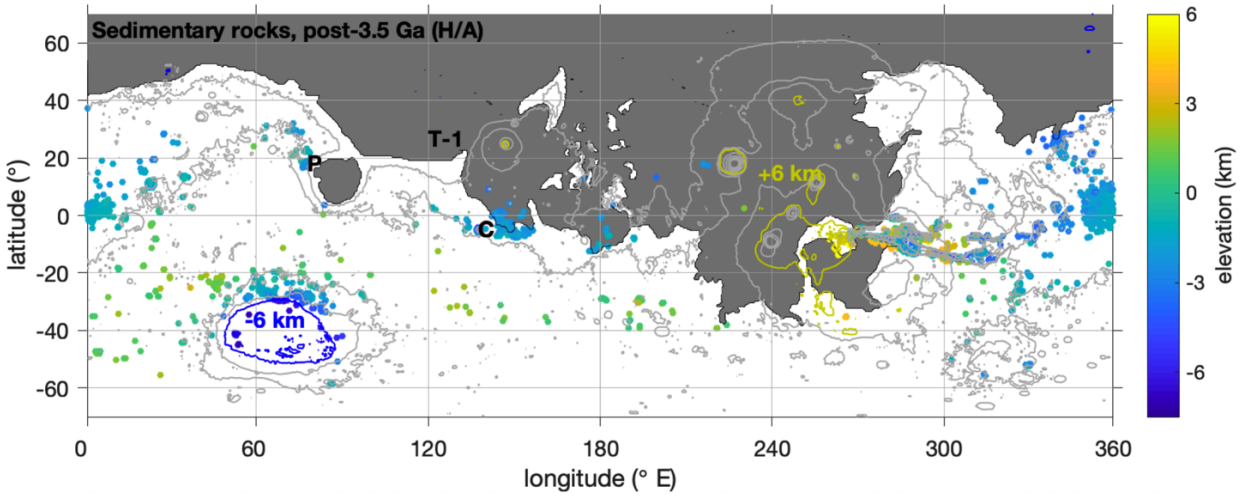

Fig. S6. Light-toned layered sedimentary rocks distribution (data from ref. *5*). Contour spacing 3 km. Gray tint: Low/no detection probability. Rovers: C = *Curiosity*, P = *Perseverance*, T-1 = *Tianwen-1* rover (*Zhurong*).

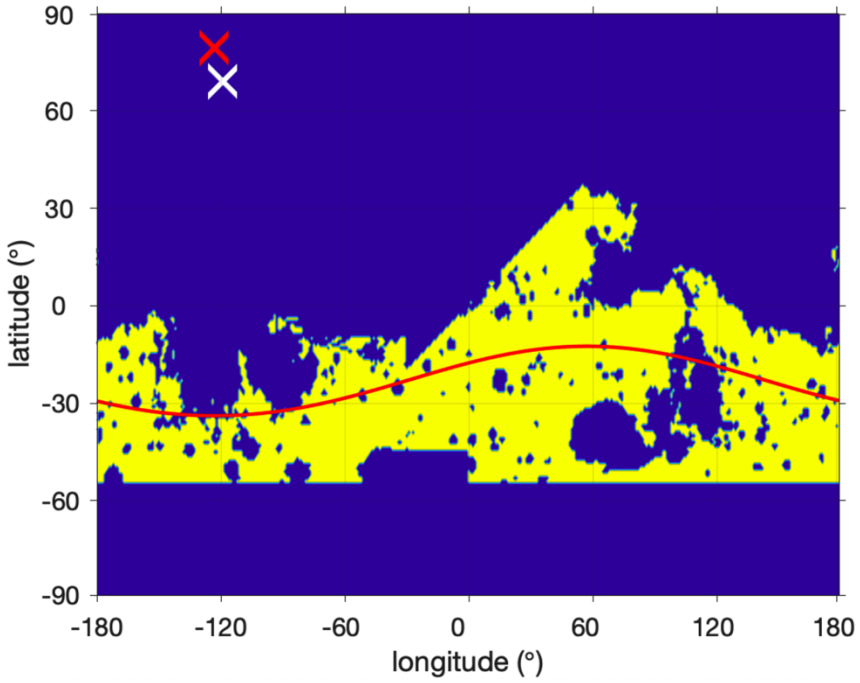

Fig. S7. Example of how a small-circle-fitting pipeline can lead to a detection of TPW when no TPW has occurred. We used a synthetic dataset in which, by construction, there is zero evidence for TPW (a uniform distribution). The resulting distribution of Valley Networks is shown in yellow and the resurfacing mask in blue. The red line shows the small circle that is the best fit to the yellow distribution, the corresponding best-fit (spurious) paleopole is shown by the red cross, and the paleopole reported by (*20*) based on Valley Network distribution is shown by the white cross.

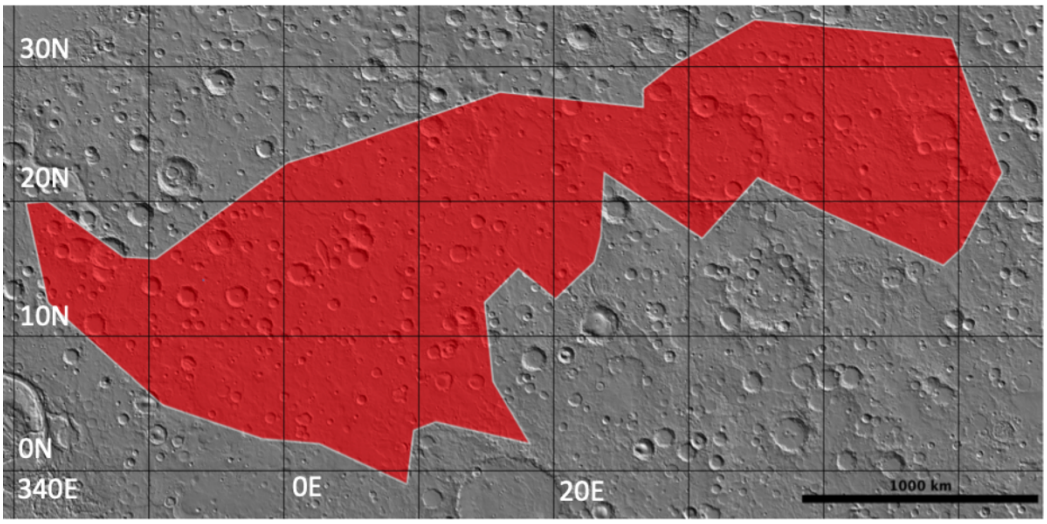

Fig. S8. Arabia Terra mask for excluding region of low/no preservation potential for valley networks, guided by the inverted-channel map of ref. *72* (their Fig. S1).

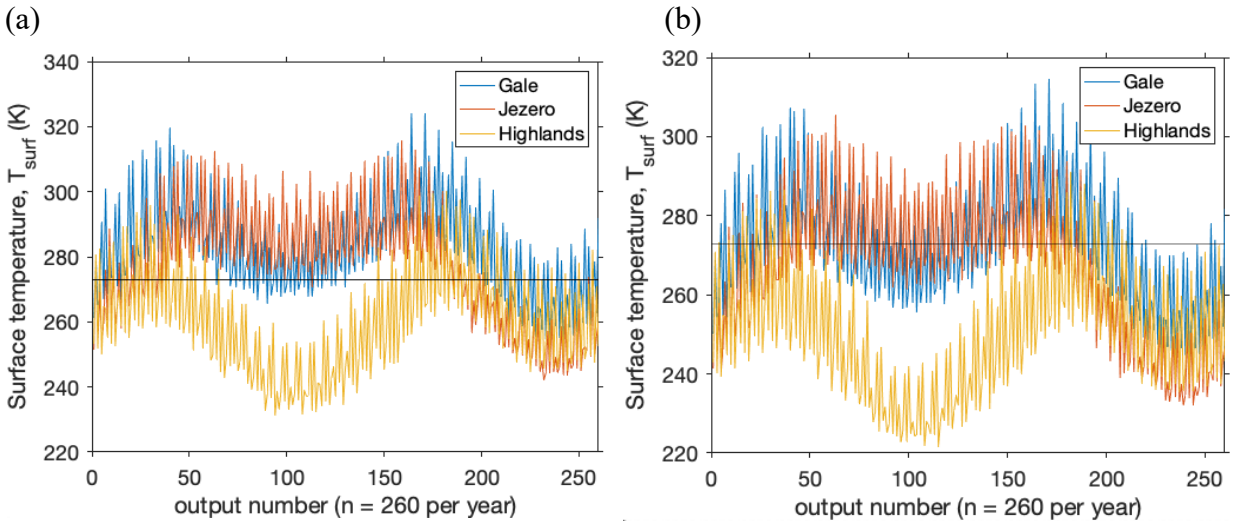

Fig. S9. (a) 260-timestep output for GCM run that best matches ~3.6 Ga data (τ = 3.14, 45° obliquity, pCO_2 = 150 mbar). Horizontal line highlights 273 K isotherm. Output is downscaled using MOLA topography. (b) As (a), but for the GCM run that best matches 3.5-3 Ga data (τ = 2.46, 45° obliquity, pCO_2 = 150 mbar). Locations within Gale crater and Jezero crater correspond to rover locations (*Curiosity* and *Perseverance*, respectively).

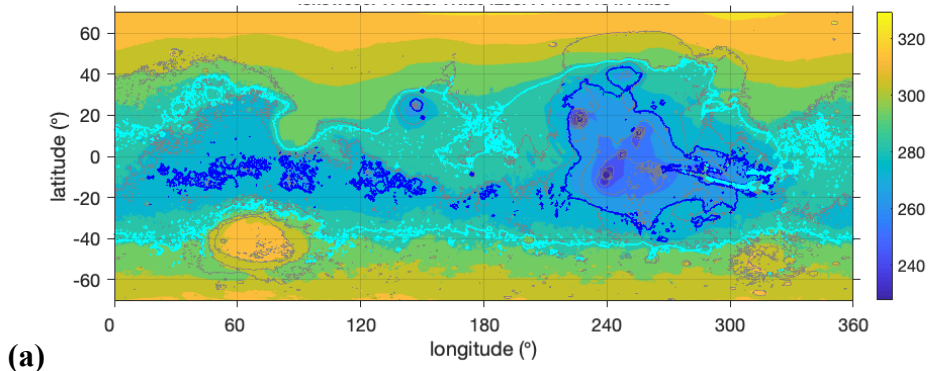
latitude (°)
longitude (°)
60
40
20
0
-20
-40
-60
0
60
120
180
240
300
360
320
300
280
260
240

(a)

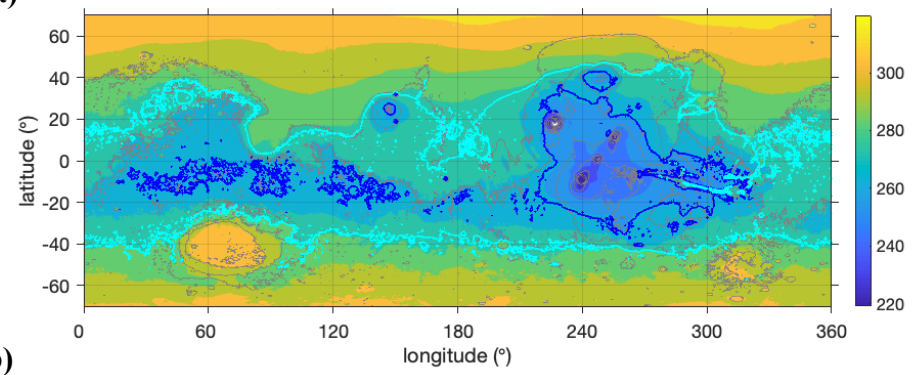
latitude (°)
longitude (°)
60
40
20
0
-20
-40
-60
0
60
120
180
240
300
360
300
280
260
240
220

(b)

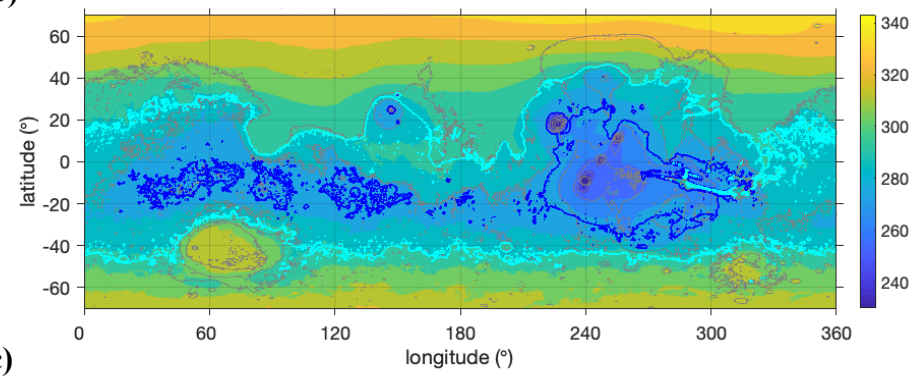
latitude (°)
longitude (°)
60
40
20
0
-20
-40
-60
0
60
120
180
240
300
360
340
320
300
280
260
240

(c)

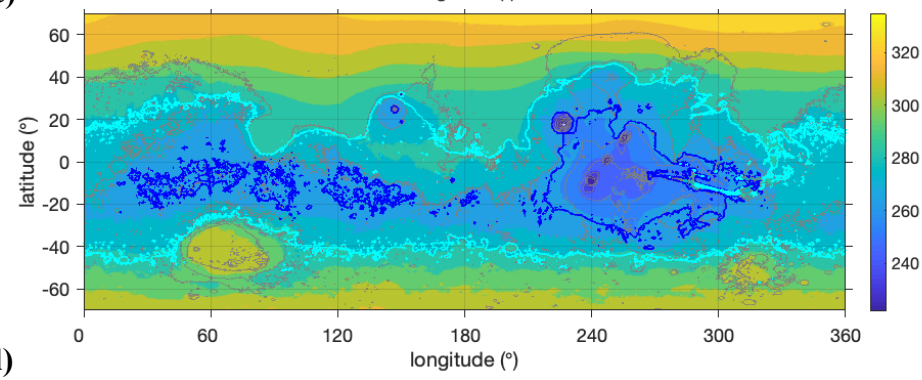
latitude (°)
longitude (°)
60
40
20
0
-20
-40
-60
0
60
120
180
240
300
360
320
300
280
260
240

(d)

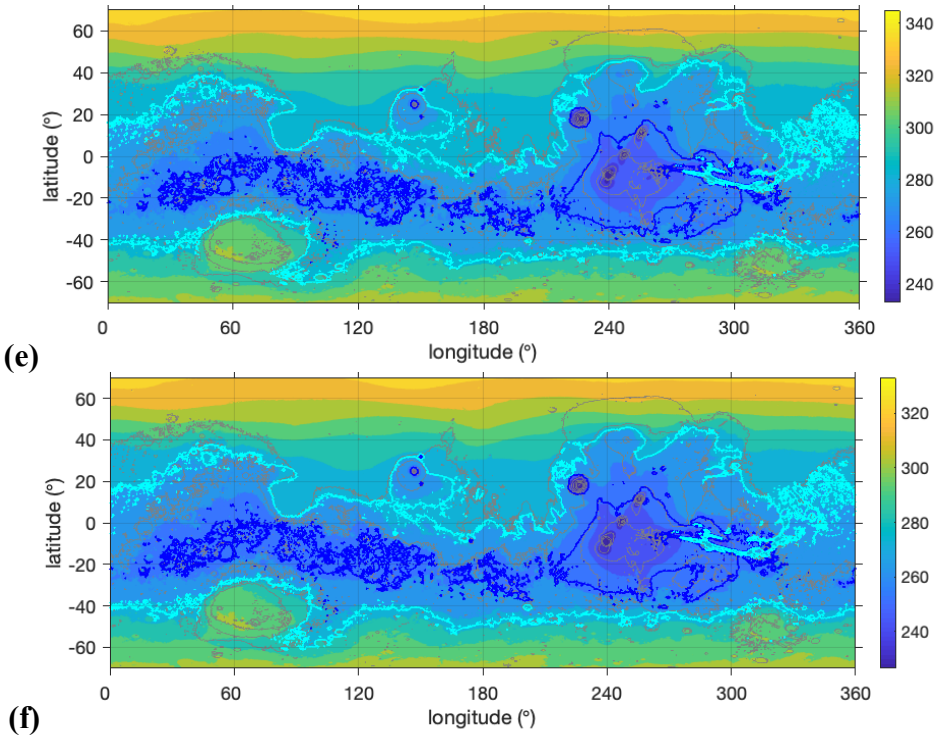

Fig. S10. As pressure decreases by a factor of 25 for constant τ, the pattern of warm-season temperatures and snowpack stability does not change much. Figure shows predicted climates for the τ values corresponding to the overall best fits shown in Figs. 3-5, but varying pCO_2 between 500 mbar, 150 mbar and 20 mbar. Colors correspond to warm-season temperature (K) (warmest 100 sols). The dark blue contours contain the part of the planet's surface area with the lowest annually integrated snow sublimation rate (0-10th percentile) , and the cyan contours contain the part of the planet's surface area with lower-than-average annually integrated snow sublimation rate (0-50th percentile). Output is downscaled using MOLA topography. Elevation contours (gray) are spaced at 3 km intervals. **(a)** τ = 3.14, 45° obliquity, pCO_2 = 500 mbar. **(b)** τ = 2.46, 45° obliquity, pCO_2 = 500 mbar. **(c)** τ = 3.14, 45° obliquity, pCO_2 = 150 mbar. **(d)** τ = 2.46, 45° obliquity, pCO_2 = 150 mbar. **(e)** τ = 3.14, 45° obliquity, pCO_2 = 20 mbar. **(f)** τ = 2.46, 45° obliquity, pCO_2 = 20 mbar.

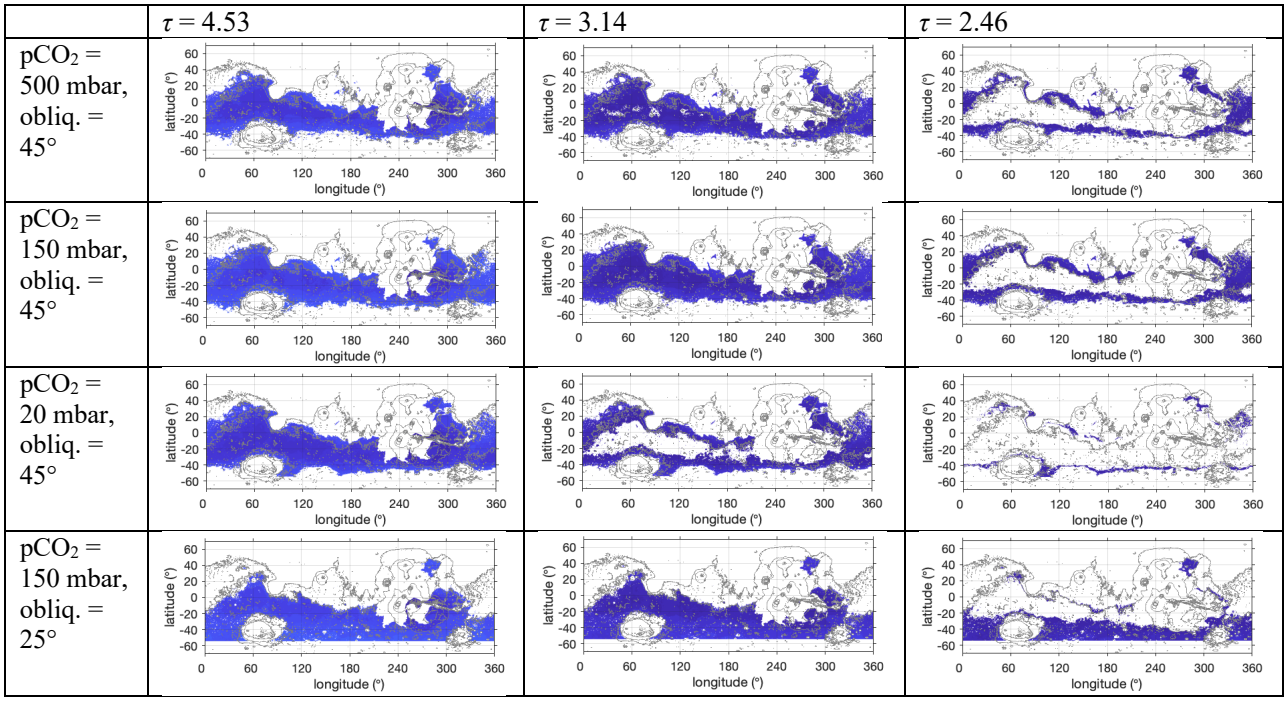

Fig. S11. The simplified meltwater predictions are only weakly sensitive to pCO_2 (row-wise variation between the first three rows), are strongly sensitive to the strength of non-CO_2 greenhouse forcing (column-wise variation), and are strongly sensitive to obliquity (fourth row), but lower obliquity predictions are a poor match to data. Geologically masked output for a fixed f_{snow} of 50%.

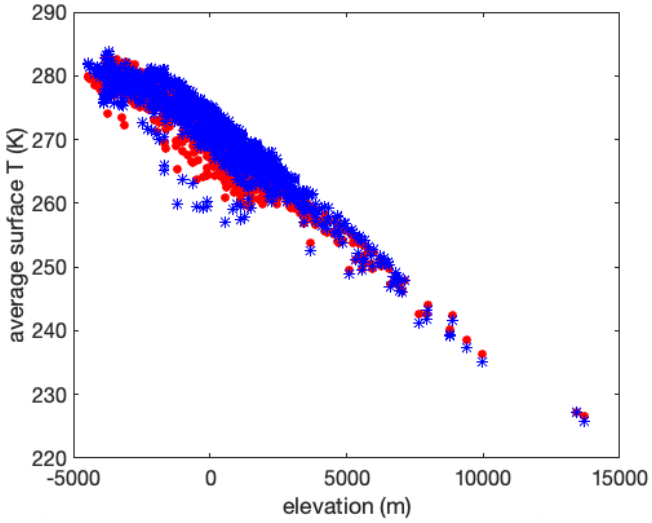

Fig. S12. The lapse rate in average surface temperature for a 500 mbar run (run 908, red dots) is almost the same as the lapse rate in average surface temperature for a 200 mbar run with the same non-CO_2 greenhouse forcing and obliquity (run 218, blue asterisks).

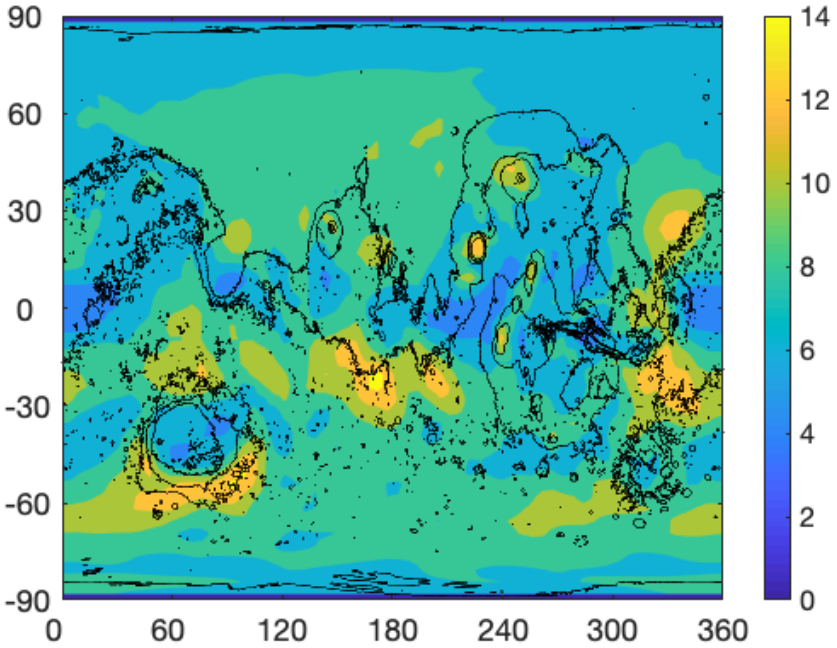

Fig. S13. Annual-average wind speed at the lowest level in the atmosphere, in m/s (for the run shown in Fig. 3a). Black contours correspond to topography and are drawn at 3 km intervals starting from -6 km.

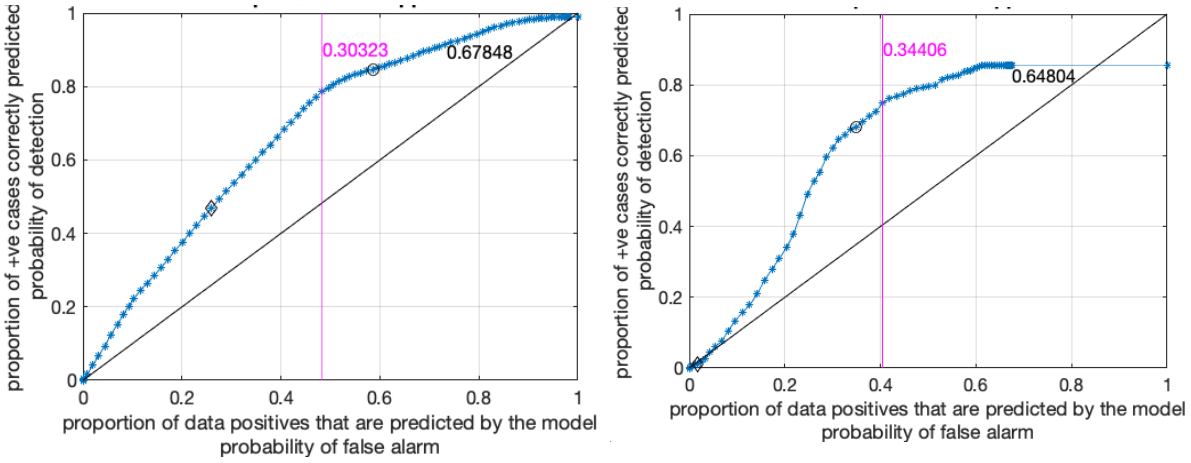

Fig. S14. Receiver operating characteristic (ROC) curves for (left) comparison of the best-fit model for >3.6 Ga data (τ = 3.14, 45° obliquity, pCO_2 = 150 mbar) to those early-stage data, (right) comparison of the best-fit model for <3.6 Ga data τ = 2.46, 45° obliquity, pCO_2 = 150 mbar to those late-stage data. Points plotting above the diagonal black line correspond to models that perform better than chance. The blue asterisks are drawn at intervals of 1% in f_{snow}. The black diamond highlights the run at f_{snow} = 25% (in each panel) and the black circle highlights the run at f_{snow} = 50% (in each panel). The vertical purple line marks the best-fit f_{snow} (with the corresponding Youden's J value in magenta). The black value in the top right is the ROC Area Under Curve (AUC).

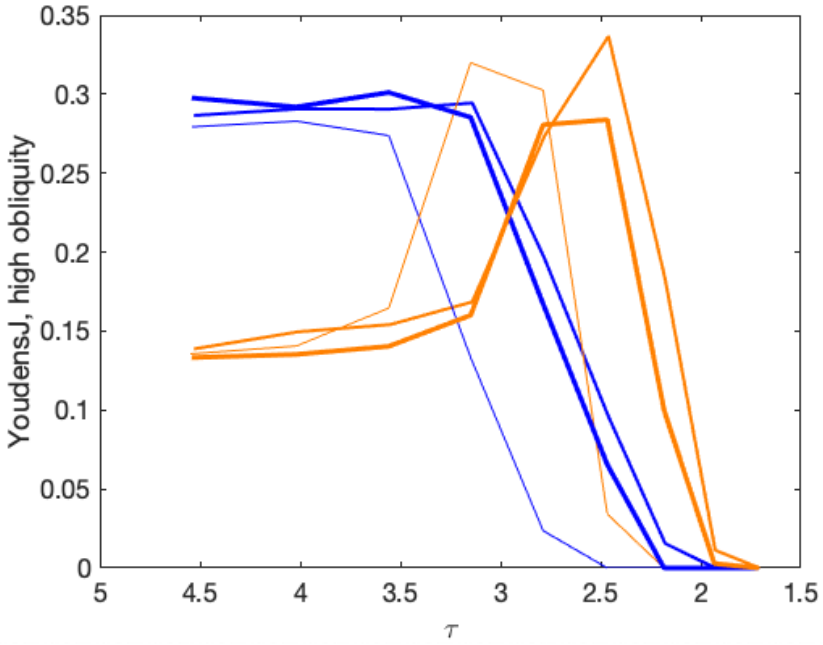

Fig. S15. Youden's J as a function of τ, comparing models to alluvial fan data (orange lines) and Valley Network data (blue lines). The thickest lines are for pCO_2 = 500 mbar, the thinnest lines are for pCO_2 = 20 mbar, and the intermediate lines are for pCO_2 = 150 mbar. The data-model comparison is relatively insensitive to pCO_2, and strongly sensitive to τ. Figure shows results for 45° obliquity.

Run ID	Input parameters			Output	Summary data-model comparison scores			
	pCO_2 (mbar)	τ	Obliq. (°)	(K)	AUC, VN era	AUC, fans era	YoudensJ, VN era	YoudensJ, fans era
215	150	4.53	45	284.8	0.6669	0.4936	0.2866	0.1387
216	150	4.01	45	278.9	0.6678	0.5031	0.2907	0.1496
217	150	3.55	45	273.3	0.6702	0.5034	0.2906	0.1542
218	150	3.14	45	267.8	0.6725	0.5211	0.2944	0.1685
219	150	2.78	45	262.7	0.5579	0.6165	0.1960	0.2735
220	150	2.46	45	257.9	0.3898	0.6613	0.0959	0.3367
225	20	4.54	45	272.7	0.6635	0.4645	0.2793	0.1356
226	20	4.02	45	267.1	0.6660	0.4711	0.2829	0.1406
227	20	3.56	45	261.7	0.6570	0.4967	0.2738	0.1646
228	20	3.15	45	256.5	0.4796	0.6413	0.1333	0.3199
229	20	2.79	45	251.5	0.2681	0.5905	0.0236	0.3025
230	20	2.47	45	248.2	0.1331	0.2320	0	0.0342
315	150	4.53	25	289.0	0.5656	0.3656	0.1022	0.0433
316	150	4.01	25	283.0	0.5656	0.3652	0.1014	0.0542
317	150	3.55	25	277.2	0.5655	0.3717	0.0977	0.0575
318	150	3.14	25	271.6	0.5641	0.3749	0.0930	0.0655
319	150	2.78	25	266.3	0.4880	0.4348	0.0201	0.1252
320	150	2.46	25	261.1	0.3485	0.5554	0	0.2529
325	20	4.54	25	277.5	0.4766	0.3416	0.0682	0.0064
326	20	4.02	25	271.4	0.4756	0.3436	0.0692	0.0127
327	20	3.56	25	265.5	0.4668	0.3640	0.0600	0.0326
328	20	3.15	25	259.8	0.3733	0.4935	-0.0003	0.1665
329	20	2.79	25	254.1	0.2038	0.5411	-0.0003	0.2352
330	20	2.47	25	248.3	0.0493	0.2178	-0.0003	-0.0000
611	150	2.18	45	253.3	0.2075	0.4577	0.0156	0.1830
612	150	1.93	45	248.9	0.1329	0.1776	0	0.0113
613	150	1.71	45	245.0	0.1103	0.0780	0	0
621	20	2.18	45	241.2	0.1030	0.0579	0	0
622	20	1.93	45	236.4	0.0755	0.0160	0	0
623	20	1.71	45	232.1	0.0545	0.0028	0	0
711	150	2.18	25	256.4	0.1983	0.5167	0	0.2222
712	150	1.93	25	251.8	0.0610	0.2074	0	0.0110
713	150	1.71	25	247.4	0.0284	0.0639	0	0
721	20	2.18	25	242.6 [†]	0.0173	0.0418	0	0
722	20	1.93	25	236.9 [†]	0.0004	0.0012	0	0
723	20	1.71	25	231.7 [†]	0	0	0	0
905	500	4.54	45	286.3	0.6694	0.4663	0.2976	0.1332
906	500	4.02	45		0.6723	0.4744	0.2919	0.1353
907	500	3.56	45	275.3	0.6772	0.4906	0.3011	0.1404
908	500	3.15	45	270.2	0.6623	0.5108	0.2854	0.1601
909	500	2.79	45	265.5	0.5209	0.6331	0.1672	0.2806
910	500	2.47	45	260.8	0.3533	0.6104	0.0655	0.2839
951	500	2.18	45	256.4	0.1899	0.3580	0.0000	0.1000
952	500	1.93	45	252.3	0.1388	0.1555	0	0.0029
953	500	1.71	45	248.3 [**]	0.1054	0.0677	0	0
1005	500	4.54	25	290.3	0.5449	0.3363	0.0882	0.0350
1006	500	4.02	25	284.8	0.5497	0.3399	0.0903	0.0430
1007	500	3.56	25	279.1	0.5509	0.3460	0.0922	0.0487
1008	500	3.15	25	273.8	0.5534	0.3540	0.0915	0.0594
1009	500	2.79	25	268.8	0.4495	0.4488	0.0016	0.1594
1010	500	2.47	25	264.0	0.3216	0.5264	0	0.2358
1051	500	2.18	25	259.3	0.1634	0.4425	0	0.1744
1052	500	1.93	25	255.0	0.0473	0.1862	0	0.0325
1053	500	1.71	25	250.9	0.0183	0.0395	0	0
401	1000	0	45	209.1	-	-	-	-
411	150	0	45	203.6	-	-	-	-
421	20	0	45	<200	-	-	-	-

Table S1. Summary of GCM output and data-model comparison.
[**] Possibly still cooling at the end of run (and much too cold to match data).
[†] Some of these extremely cold 20 mbar runs show evidence for ongoing atmospheric collapse.

REFERENCES AND NOTES

1. J. P. Grotzinger, D. Y. Sumner, L. C. Kah, K. Stack, S. Gupta, L. Edgar, D. Rubin, K. Lewis, J. Schieber, N. Mangold, R. Milliken, P. G. Conrad, D. DesMarais, J. Farmer, K. Siebach, F. Calef III, J. Hurowitz, S. M. McLennan, D. Ming, D. Vaniman, J. Crisp, A. Vasavada, K. S. Edgett, M. Malin, D. Blake, R. Gellert, P. Mahaffy, R. C. Wiens, S. Maurice, J A Grant, S. Wilson, R. C. Anderson, L. Beegle, R. Arvidson, B. Hallet, R S Sletten, M. Rice, J. Bell III, J. Griffes, B. Ehlmann, R B Anderson, T. F. Bristow, W. E. Dietrich, G. Dromart, J. Eigenbrode, A. Fraeman, C. Hardgrove, K. Herkenhoff, L. Jandura, G. Kocurek, S. Lee, L. A. Leshin, R. Leveille, D. Limonadi, J. Maki, S McCloskey, M. Meyer, M. Minitti, H. Newsom, D. Oehler, A. Okon, M. Palucis, T. Parker, S. Rowland, M. Schmidt, S. Squyres, A. Steele, E. Stolper, R. Summons, A. Treiman, R. Williams, A. Yingst; MSL Science Team, A habitable fluvio-lacustrine environment at Yellowknife Bay, Gale crater, Mars, *Science* **343**, 1242777 (2014).

2. R. P. Irwin, K. W. Lewis, A. D. Howard, J. A. Grant, Paleohydrology of Eberswalde crater, Mars, *Geomorphology* **240**, 83–101 (2015).

3. J. A. Grant, S. A. Wilson, Late alluvial fan formation in southern Margaritifer Terra, Mars, *Geophys. Res. Lett.* **38**, L08201 (2011).

4. E. S. Kite, Geologic constraints on Early Mars climate. *Space Sci. Rev.* **215**, 10 (2019).

5. A. P. Ingersoll, Mars: Occurrence of liquid water. *Science* **168**, 972–973 (1970).

6. B. M. Jakosky, D. Brain, M. Chaffin, S. Curry, J. Deighan, J. Grebowsky, J. Halekas, F. Leblanc, R. Lillis, J. G. Luhmann, L. Andersson, N. Andre, D. Andrews, D. Baird, D. Baker, J. Bell, M. Benna, D. Bhattacharyya, S. Bougher, C. Bowers, P. Chamberlin, J. Y. Chaufray, J. Clarke, G. Collinson, M. Combi, J. Connerney, K. Connour, J. Correira, K. Crabb, F. Crary, T. Cravens, M. Crismani, G. Delory, R. Dewey, G. DiBraccio, C. Dong, Y. Dong, P. Dunn, H. Egan, M. Elrod, S. England, F. Eparvier, R. Ergun, A. Eriksson, T. Esman, J. Espley, S. Evans, K. Fallows, X. Fang, M. Fillingim, C. Flynn, A. Fogle, C. Fowler, J. Fox, M. Fujimoto, P. Garnier, Z. Girazian, H. Groeller, J. Gruesbeck, O. Hamil, K. G. Hanley, T. Hara, Y. Harada, J. Hermann, M. Holmberg, G. Holsclaw, S. Houston, S. Inui, S. Jain, R. Jolitz, A. Kotova, T. Kuroda, D. Larson, Y. Lee, C. Lee, F. Lefevre, C.

Lentz, D. Lo, R. Lugo, Y. J. Ma, P. Mahaffy, M. L. Marquette, Y. Matsumoto, M. Mayyasi, C. Mazelle, W. McClintock, J. McFadden, A. Medvedev, M. Mendillo, K. Meziane, Z. Milby, D. Mitchell, R. Modolo, F. Montmessin, A. Nagy, H. Nakagawa, C. Narvaez, K. Olsen, D. Pawlowski, W. Peterson, A. Rahmati, K. Roeten, N. Romanelli, S. Ruhunusiri, C. Russell, S. Sakai, N. Schneider, K. Seki, R. Sharrar, S. Shaver, D. E. Siskind, M. Slipski, Y. Soobiah, M. Steckiewicz, M. H. Stevens, I. Stewart, A. Stiepen, S. Stone, V. Tenishev, N. Terada, K. Terada, E. Thiemann, R. Tolson, G. Toth, J. Trovato, M. Vogt, T. Weber, P. Withers, S. Xu, R. Yelle, E. Yiğit, R. Zurek, Loss of the Martian atmosphere to space: Present-day loss rates determined from MAVEN observations and integrated loss through time. *Icarus* **315**, 146–157 (2018).

7. R. M. Haberle, D. C. Catling, M. H. Carr, K. J. Zahnle, The Early Mars Climate System, in *The Atmosphere and Climate of Mars*, R. M. Haberle, R. T. Clancy, F. Forget, M. D. Smith, R. W. Zurek, Eds. (Cambridge Univ. Press, 2017), pp. 497–525.

8. D. C. Catling, J. F. Kasting, *Atmospheric Evolution on Inhabited and Lifeless Worlds* (Cambridge Univ. Press, 2017).

9. R. Wordsworth, F. Forget, E. Millour, J. W. Head, J.-B. Madeleine, B. Charnay, Global modelling of the early martian climate under a denser CO_2 atmosphere: Water cycle and ice evolution. *Icarus* **222**, 1–19 (2013).

10. C. I. Fassett, J. W. Head, The timing of martian valley network activity: Constraints from buffered crater counting, *Icarus*, **195**, 61–89 (2008).

11. E. S. Kite, J. Sneed, D. P. Mayer, S. A. Wilson, Persistent or repeated surface habitability on Mars during the late Hesperian–Amazonian, *Geophys. Res. Lett.* **44**, 3991–3999 (2017).

12. P. B. Buhler, Timescales of fluvial activity and intermittency in Milna Crater, Mars. *Icarus* **241**, 130–147 (2014).

13. M. G. A. Lapôtre, A. Ielpi, The pace of fluvial meanders on Mars and implications for the western delta deposits of Jezero crater, *AGU Adv.* **1**, e2019AV000141 (2020).

14. R. E. Milliken, R. C. Ewing, W. W. Fischer, J. Hurowitz, Wind-blown sandstones cemented by sulfate and clay minerals in Gale Crater, Mars. *Geophys. Res. Lett.* **41**, 1149–1154 (2014).

15. W. Rapin, G. Dromart, D. Rubin, L. Le Deit, N. Mangold, L. A. Edgar, O. Gasnault, K. Herkenhoff, S. Le Mouélic, R. B. Anderson, S. Maurice, V. Fox, B. L. Ehlmann, J. L. Dickson, R. C. Wiens, Alternating wet and dry depositional environments recorded in the stratigraphy of Mount Sharp at Gale crater, Mars. *Geology* **49**, 842–846 (2021).

16. R. A. Craddock, T. A. Maxwell, Geomorphic evolution of the Martian highlands through ancient fluvial processes. *J. Geophys. Res. Planets* **98**, 3453–3468 (1993).

17. B. M. Hynek, M. Beach, M. R. T. Hoke, Updated global map of Martian valley networks and implications for climate and hydrologic processes. *J. Geophys. Res. Planets* **115**, E09008 (2010).

18. S. A. Wilson, A. M. Morgan, A. D. Howard, J. A. Grant, The global distribution of craters with alluvial fans and deltas on Mars. *Geophys. Res. Lett.* **48**, e2020GL091653 (2021).

19. M. Turbet, F. Forget, 3-D Global modelling of the early martian climate under a dense CO_2+H_2 atmosphere and for a wide range of surface water inventories. arXiv:2103.10301 [astro-ph.EP] (18 March 2021).

20. S. Bouley, D. Baratoux, I. Matsuyama, F. Forget, A. Séjourné, M. Turbet, F. Costard, Late Tharsis formation and implications for early Mars. *Nature* **531**, 344–347 (2016).

21. K. E. Scanlon, J. W. Head, J. L. Fastook, R. D. Wordsworth, The Dorsa Argentea formation and the Noachian-Hesperian climate transition. *Icarus* **299**, 339–363 (2018).

22. N. R. Alsaeed, B. M. Jakosky, Mars water and D/H evolution from 3.3 Ga to present, *J. Geophys. Res. Planets* **124**, 3344–3353 (2019).

23. M. I. Richardson, A. D. Toigo, C. E. Newman, PlanetWRF: A general purpose, local to global numerical model for planetary atmospheric and climate dynamics. *J. Geophys. Res.* **112**, E09001 (2007).

24. A. D. Toigo, C. Lee, C. E. Newman, M. I. Richardson, The impact of resolution on the dynamics of the Martian global atmosphere: Varying resolution studies with the MarsWRF GCM. *Icarus* **221**, 276–288 (2012).

25. R. D. Wordsworth, L. Kerber, R. T. Pierrehumbert, F. Forget, J. W. Head, Comparison of "warm and wet" and "cold and icy" scenarios for early Mars in a 3-D climate model. *J. Geophys. Res. Planets* **120** 1201–1219 (2015).

26. A. M. Palumbo, J. W. Head, Early Mars climate history: Characterizing a "warm and wet" martian climate with a 3-D global climate model and testing geological predictions. *Geophys. Res. Lett.* **45**, 10249–10258 (2018).

27. J. N. Bahcall, M. H. Pinsonneault, S. Basu Solar models: Current epoch and time dependences, neutrinos, and helioseismological properties. *Astrophys. J.* **555**, 990–1012 (2001).

28. C. I. Fassett, J. L. Dickson, J. W. Head, J. S. Levy, D. R. Marchant, Supraglacial and proglacial valleys on Amazonian Mars. *Icarus* **208**, 86–100 (2010).

29. E. S. Kite, I. Halevy, M. A. Kahre, M. J. Wolff, M. Manga, Seasonal melting and the formation of sedimentary rocks on Mars, with predictions for the Gale Crater mound. *Icarus* **223**, 181–210 (2013).

30. G. D. Clow, Generation of liquid water on Mars through the melting of a dusty snowpack. *Icarus* **72**, 95–127 (1987).

31. R. A. Wharton Jr, C. P. McKay, G. D. Clow, D. T. Andersen, G. M. Simmons Jr., F. G. Love, Changes in ice cover thickness and lake level of Lake Hoare, Antarctica: Implications for local climatic change. *J. Geophys. Res. Oceans* **97**, 3503–3513 (1992).

32. P. T. Doran, C. P. McKay, A. G. Fountain, T. Nylen, D. M. McKnight, C. Jaros, J. E. Barrett, Hydrologic response to extreme warm and cold summers in the McMurdo Dry Valleys, East Antarctica. *Antarct. Sci.* **20**, 499–509 (2008).

33. M. A. Mischna, V. Baker, R. Milliken, M. Richardson, C. Lee, Effects of obliquity and water vapor/trace gas greenhouses in the early Martian climate. *J. Geophys. Res. Planets* **118**, 560–576 (2013).

34. R. Ramirez, R. Craddock, The geological and climatological case for a warmer and wetter early Mars. *Nat. Geosci.* **11**, 230–237 (2018).

35. J. C. Andrews-Hanna, M. T. Zuber, R. E. Arvidson, S. M. Wiseman, Early Mars hydrology: Meridiani playa deposits and the sedimentary record of Arabia Terra. *J. Geophys. Res.* **115**, E06002 (2010).

36. S. D. Guzewich, M. J. Way, I. Aleinov, E. T. WolfAnthony, A. Del Genio, R. Wordsworth, K. Tsigaridis, 3D simulations of the early martian hydrological cycle mediated by a H_2-CO_2 greenhouse. *J. Geophys. Res. Planets* **126,** (2021).

37. R. K. Kopparapu, R. Ramirez, J. F. Kasting, V. Eymet, T. D. Robinson, S. Mahadevan, R. C. Terrien, S. Domagal-Goldman, V. Meadows, R. Deshpande, Habitable zones around main-sequence stars: New estimates. *Astrophys. J.* **765**, 131 (2013).

38. M. Turbet, C. Boulet, T. Karman, Measurements and semi-empirical calculations of CO_2 + CH_4 and CO_2 + H_2 collision-induced absorption across a wide range of wavelengths and temperatures. Application for the prediction of early Mars surface temperature. *Icarus* **346**, 113762 (2020).

39. A. Palumbo, J. W. Head, Groundwater release on early Mars: Utilizing models and proposed evidence for groundwater release to estimate the required climate and subsurface water budget. *Geophys. Res. Lett.* **47**, e87230 (2020).

40. A. R. Khuller, P. R. Christensen, S. G. Warren, Spectral albedo of dusty martian H_2O snow and ice. *J. Geophys. Res. Planets* **126**, e2021JE006910 (2021).

41. P. R. Mahaffy, C. R. Webster, J. C. Stern, A. E. Brunner, S. K. Atreya, P. G. Conrad, S. Domagal-Goldman, J. L. Eigenbrode, G. J. Flesch, L. E. Christensen, H. B. Franz, C. Freissinet, D. P. Glavin, J. P. Grotzinger, J. H. Jones, L. A. Leshin, C. Malespin, A. C. McAdam, D. W. Ming, R. Navarro-Gonzalez, P. B. Niles, T. Owen, A. A. Pavlov, A. Steele, M. G. Trainer, K. H. Williford, J. J. Wray;

MSL Science Team, The imprint of atmospheric evolution in the D/H of Hesperian clay minerals on Mars. *Science* **347**, 412–414 (2015).

42. S. J. Holo, E. S. Kite, S. A. Wilson, A. M. Morgan, The timing of alluvial fan formation on Mars. *Planet. Sci. J.* **2**, 210 (2021).

43. D. Y. Lo, R. V. Yelle, R. J. Lillis, J. I. Deighan, Carbon photochemical escape rates from the modern Mars atmosphere. *Icarus* **360**, 114371 (2021).

44. C. R. Webster, P. R. Mahaffy, G. J. Flesch, P. B. Niles, J. H. Jones, L. A. Leshin, S. K. Atreya, J. C. Stern, L. E. Christensen, T. Owen, H. Franz, R. O. Pepin, A. Steele; MSL Science Team, Isotope ratios of H, C, and O in CO_2 and H_2O of the Martian atmosphere. *Science* **341**, 260–263 (2013).

45. T. Owen, A. Bar-Nun, Comets, impacts, and atmospheres. *Icarus* **116**, 215–226 (1995).

46. R. M. Ramirez, R. Kopparapu, M. E. Zugger, T. D. Robinson, R. Freedman, J. F. Kasting, Warming early Mars with CO_2 and H_2. *Nat. Geosci.* **7**, 59–63 (2014).

47. R. Wordsworth, Y. Kalugina, S. Lokshtanov, A. Vigasin, B. Ehlmann, J. Head, C. Sanders, H. Wang, Transient reducing greenhouse warming on early Mars. *Geophys. Res. Lett.* **44**, 665–671 (2017).

48. R. A. Urata, O. B. Toon, Simulations of the Martian hydrologic cycle with a general circulation model: Implications for the ancient Martian climate. *Icarus* **226**, 229–250 (2013).

49. E. S. Kite, L. J. Steele, M. A. Mischna, M. I. Richardson, Warm early Mars surface enabled by high-altitude water ice clouds. *Proc. Natl. Acad. Sci. U.S.A.* **118**, e2101959118 (2021).

50. B. H. N. Horgan, R. B. Anderson, G. Dromart, E. S. Amador, M. S. Rice, The mineral diversity of Jezero crater: Evidence for possible lacustrine carbonates on Mars. *Icarus* **339**, 113526 (2020).

51. B. L. Ehlmann, C. S. Edwards, Mineralogy of the Martian surface. *Annu. Rev. Earth Planet. Sci.* **42**, 291–315 (2014).

52. M. P. Lamb, A. D. Howard, J. Johnson, K. X. Whipple, W. E. Dietrich, J. T. Perron, Can springs cut canyons into rock? *J. Geophys. Res.* **111**, E07002 (2006).

53. E. R. Kraal, M. van Dijk, G. Postma, M. G. Kleinhans, Martian stepped-delta formation by rapid water release. *Nature* **451**, 973–976 (2008).

54. M. G. A. Lapôtre, M. P. Lamb, Substrate controls on valley formation by groundwater on Earth and Mars. *Geology* **46**, 531–534 (2018).

55. E. Hauber, T. Platz, D. Reiss, L. le Deit, M. G. Kleinhans, W. A. Marra, T. de Haas, P. Carbonneau, Asynchronous formation of Hesperian and Amazonian-aged deltas on Mars and implications for climate. *J. Geophys. Res.* **118**, 1529–1544 (2013).

56. M. Turbet, C. Gillmann, F. Forget, B. Baudin, A. Palumbo, J. Head, O. Karatekin, The environmental effects of very large bolide impacts on early Mars explored with a hierarchy of numerical models. *Icarus* **335**, 113419 (2020).

57. R. M. Haberle, K. Zahnle, N. G. Barlow, K. E. Steakley, Impact degassing of H_2 on Early Mars and its effect on the climate system. *Geophys. Res. Lett.* **46**, 13355–13362 (2019).

58. K. Goddard, N. H. Warner, S. Gupta, J.-R. Kim, Mechanisms and timescales of fluvial activity at Mojave and other young Martian craters. *J. Geophys. Res. Planets* **119**, 604–634 (2014).

59. D. K. Weiss, J. W. Head, Extensive Amazonian-aged fluvial channels on Mars: Evaluating the role of Lyot crater in their formation. *Geophys. Res. Lett.* **44**, 5336–5344 (2017).

60. C. M. Dundas, A. S. McEwen, S. Diniega, C. J. Hansen, S. Byrne, J. N. McElwaine, The formation of gullies on Mars today, in *Martian Gullies and Their Earth Analogues*, S. J. Conway, J. L. Carrivick, P. A. Carling, T. De Haas, T. N. Harrison, Eds. (Geological Society, 2017), pp. 67–94, vol. 467.

61. S. W. Squyres, J. F. Kasting, Early Mars: How warm and how wet? *Science* **265**, 744–749 (1994).

62. E. S. Kite, D. P. Mayer, S. Wilson, J. Davis, A. S. Lucas, G. Stucky de Quay, Persistence of intense, climate-driven runoff late in Mars history. *Sci. Adv.* **5**, eaav7710 (2019).

63. T. A. Goudge, C. I. Fassett, J. W. Head, J. F. Mustard, K. L. Aureli, Insights into surface runoff on early Mars from paleolake basin morphology and stratigraphy. *Geology* **44**, 419–422 (2016).

64. J. M. Moore, A. D. Howard, Large alluvial fans on Mars. *J. Geophys. Res. Planets* **110** E04005 (2005).

65. M. Mangold, G. Dromart, V. Ansan, F. Salese, M. G. Kleinhans, M. Massé, C. Quantin, K. M. Stack, Fluvial regimes, morphometry, and age of Jezero crater paleolake inlet valleys and their exobiological significance for the 2020 Rover Mission Landing Site. *Astrobiology* **20**, 994–1013 (2020).

66. G. G. Michael Planetary surface dating from crater size-frequency distribution measurements: Multiple resurfacing episodes and differential isochron fitting. *Icarus* **226**, 885–890 (2013).

67. W. Luo, X. Cang, A. D. Howard, New Martian valley network volume estimate consistent with ancient ocean and warm and wet climate. *Nat. Commun.* **8**, 15766 (2017).

68. E. R. Kraal, E. Asphaug, J. M. Moore, A. Howard, A. Bredt, Catalogue of large alluvial fans in Martian impact craters. *Icarus* **194**, 101–110 (2008).

69. K. L. Tanaka, J. A. Skinner Jr., J. M. Dohm, R. P. Irwin III, E. J. Kolb, C. M. Fortezzo, T. Platz, G. G. Michael, T. M. Hare, Geologic map of Mars: USGS Scientific Investigations Map 3292 (2014).

70. F. Nimmo, K. Tanaka, Early crustal evolution of Mars. *Annu. Rev. Earth Planet. Sci.* **33**, 133–161 (2005).

71. D. E. Smith, M. T. Zuber, H. V. Frey, J. B. Garvin, J. W. Head, D. O. Muhleman, G. H. Pettengill, R. J. Phillips, S. C. Solomon, H. J. Zwally, W. B. Banerdt, T. C. Duxbury, M. P. Golombek, F. G. Lemoine, G. A. Neumann, D. D. Rowlands, O. Aharonson, P. G. Ford, A. B. Ivanov, C. L. Johnson, Patrick J. Mc Govern, J. B. Abshire, R. S. Afzal, X. Sun, Mars orbiter laser altimeter: Experiment summary after the first year of global mapping of Mars. *J. Geophys. Res.* **106**, 23689–23722 (2001).

72. T. A. Goudge, C. I. Fassett, J. W. Head, J. F. Mustard, K. L. Aureli, Extensive Noachian fluvial systems in Arabia Terra: Implications for early Martian climate. *Geology* **44**, 847–850 (2016).

73. M. A. Kreslavsky, J. W. Head, Mars climate history: Insights from impact crater wall slope statistics. *Geophys. Res. Lett.* **45**, 1751–1758 (2018).

74. R. M. E. Williams, R. J. Phillips, Morphometric measurements of martian valley networks from Mars Orbiter Laser Altimeter (MOLA) data, *J. Geophys. Res.* **106**, 23737–23751 (2001).

75. R. E. Grimm, S. C. Solomon, Tectonic tests of proposed polar wander paths for Mars and the Moon. *Icarus* **65**, 110–121 (1986).

76. R. I. Citron, M. Manga, D. J. Hemingway, Timing of oceans on Mars from shoreline deformation. *Nature* **555**, 643–646 (2018).

77. M. C. Malin, K. S. Edgett, B. A. Cantor, M. A. Caplinger, G. E. Danielson, E. H. Jensen, M. A. Ravine, J. L. Sandoval, K. D. Supulver, An overview of the 1985–2006 Mars Orbiter Camera science investigation. *Int. J. Mars Sci. Explor.* **4**, 1–60 (2010).

78. R. Beyer, K. Stack, J. L. Griffes, R. E. Milliken, K. E. Herkenhoff, S. Byrne, J. W. Holt, J. P. Grotzinger, An atlas of Mars sedimentary rocks as seen by HiRISE, in *Sedimentary Geology of Mars*, J. P. Grotzinger, R. E. Milliken, Eds. (SEPM Special Publication No. 102, 2012).

79. M. A. Mischna, C. Lee, M. Richardson, Development of a fast, accurate radiative transfer model for the Martian atmosphere, past and present. *J. Geophys. Res.* **117** E10009 (2012).

80. R. M. Ramirez, J. F. Kasting Could cirrus clouds have warmed early Mars? *Icarus* **281**, 248–261 (2017).

81. C. M. Dundas, S. Byrne Modeling sublimation of ice exposed by new impacts in the martian mid-latitudes. *Icarus* **206**, 716–728 (2010).

82. W. J. Youden, Index for rating diagnostic tests. *Cancer* **3**, 32–35 (1950).